Defects at grain boundaries: A coarse-grained, three-dimensional description by the amplitude expansion of the phase-field crystal model

Marco Salvalaglio, Rainer Backofen, K. R. Elder, and Axel Voigt

Phys. Rev. Materials **2**, 053804 — Published 30 May 2018

DOI: 10.1103/PhysRevMaterials.2.053804

Defects at grain boundaries: a coarse-grained, three-dimensional description by the amplitude expansion of the phase-field crystal model

Marco Salvalaglio,[1,*] Rainer Backofen,[1] K. R. Elder,[2] and Axel Voigt[1,3]

[1] *Institute of Scientific Computing, Technische Universität Dresden, 01062 Dresden, Germany*
[2] *Department of Physics, Oakland University, Rochester, 48309 Michigan, USA.*
[3] *Dresden Center for Computational Materials Science (DCMS), TU Dresden, 01062 Dresden, Germany*

We address a three-dimensional, coarse-grained description of dislocation networks at grain boundaries between rotated crystals. The so-called amplitude expansion of the phase-field crystal model is exploited with the aid of Finite Element Method calculations. This approach allows for the description of microscopic features, such as dislocations, while simultaneously being able to describe length scales that are orders of magnitude larger than the lattice spacing. Moreover, it allows for the direct description of extended defects by means of a scalar order parameter. The versatility of this framework is shown by considering both fcc and bcc lattice symmetries and different rotation axes. First, the specific case of planar, twist grain boundaries is illustrated. The details of the method are reported and the consistency of the results with literature is discussed. Then, the dislocation networks forming at the interface between a spherical, rotated crystal embedded in an unrotated crystalline structure, are shown. Although explicitly accounting for dislocations which lead to an anisotropic shrinkage of the rotated grain, the extension of the spherical grain boundary is found to decrease linearly over time in agreement with the classical theory of grain growth and recent atomistic investigations. It is shown that the results obtained for a system with bcc symmetry agree very well with existing results, validating the methodology. Furthermore, fully original results are shown for fcc lattice symmetry, revealing the generality of the reported observations.

I. INTRODUCTION

Grain boundaries (GBs) are interfaces between crystal grains having different orientations. They consist of extended, two-dimensional defects and determine several features of polycrystalline materials such as mechanical and ferromagnetic properties as well as thermal and electrical conductivity[1]. The migration of GBs determines the microstructure evolution in polycrystalline materials[2] and consequently it is crucial to develop an in-depth understanding of such motion for controlling and tuning material properties[3].

The description of GB morphologies and dynamics is a typical mesoscale problem[4]. Indeed, networks of one-dimensional, extended defects, i.e. dislocations, form at the interfaces between crystals with different orientations[1]. Their nature, motion and reaction, in turn, strictly depends on microscopic features such as the atom packing along crystallographic planes or the concentration of vacancies[5]. The importance of GBs and their influence on microstructural behavior in a wide range of polycrystalline materials, from metals and semiconductors[6,7] to ionic and organic crystals[8,9], make them a central topic for material science investigations. Indeed, the study of GBs fostered the development of several experimental and theoretical techniques working at different length scales[4].

Regarding theory and modeling, many of the available methods from the atomic to the continuum length-scale has been adopted in order to provide both a deep understanding of experiments and insights on the GB behaviors under ideal conditions. Continuum modeling shed first light on the basics of GB energetics, motion and morphology[10,11]. Macroscopic simulations of microstructures evolution has been used to address the dynamics of GBs as a continuous interface between grains, e.g. by phase- and multiphase-field approaches[12–14] or by continuum mechanics simulations accounting for plasticity[15]. Microscopic methods such as Molecular Dynamics (MD) or Monte-Carlo approaches have been used to provide atomic-level insights on GBs and parameters for mesoscale or macroscopic modeling[16–20]. The so-called Phase-Field Crystal (PFC) method[21–23] provides a description of the atomic probability density on the diffusive timescale and filters out the dynamics of vibrations. This approach has been extensively used to provide long-timescale descriptions of GBs and dislocation dynamics[24–26].

While each of these methods is a viable tool for the investigation of GBs, they have limitations. For instance, MD is restricted to relatively short timescales limiting the application to long timescale processes, PFC requires a fine spatial discretization allowing for the simulation of relatively small systems and many continuum approaches are missing the essential physical properties of GBs. Therefore, multiscale methods or coarse-grained approaches, bridging the gap between the range of applicability of these techniques, would be highly desirable to provide general information on polycrystalline materials.

The so-called Amplitude Expansion of the PFC model (APFC) offers a coarse-grained description able to account for atomistic details at lengthscales typical of classical phase-field (or in general continuum) approaches[27–29]. The periodic atomic probability density described by PFC is accounted for by means of the minimum set of Fourier modes or plane waves required by a given crystal-lattice symmetry. Then the evolution of the complex amplitudes of such waves, η_j, is described under

the approximation of slowly varying amplitude functions, i.e. varying on a larger lengthscale than the lattice spacing. Complex amplitude functions allow for describing rotations and deformations of the lattice structure. In addition, by means of η_j's it is also possible to compute a scalar order parameter (referred to as A^2 in the following) that is maximum within the crystal, decreases at defects and at crystal-melt or ordered-disordered interfaces and vanishes for disordered-liquid phases. So that it can be thought of as being related to the order parameter that enters standard phase-field approaches. Although the APFC approach does not provide an accurate description of the atomic rearrangement at dislocation cores, it is known to give good coarse-grained approximations of PFC for small deformations or tilts and has been already adopted to investigate GBs in two dimensions[24,30–32]. Moreover, the original model has been extended to binary systems and to body-centered cubic (bcc) and face-centered cubic (fcc) symmetries[33,34]. The possibility to tune interface and defect energies has been also recently shown[35]. Except for some proof of concepts, no three-dimensional (3D) simulations were provided. However, in Ref.[35] a unified description of different lattice symmetries and a numerical scheme able to cope with 3D systems were discussed, paving the way to advanced simulations of material properties.

In this work, by exploiting the framework reported in Ref.[35], we address the 3D description of defect structures forming at the interface between rotated crystals by APFC. A coarse-grained description of dislocation networks, achieved without explicitly considering the atoms of the crystal lattice, is then provided. It is proved to account for the specific lattice symmetry, the rotation axis, and the geometry of the interface between crystals. The final goal of this paper is to illustrate defect morphologies forming between a spherical, rotated grain in an unrotated lattice and their evolution. Indeed, this is a prototypical system where all the possible orientations of a GB with respect to the rotation axis are present. Moreover, it evolves until the disappearance of the rotated grain and can be compared with classical continuum theory[36] and atomistic calculations[26].

To this purpose, we first tackle the modeling of planar, twist GBs. This allows us to assess the general approach and show the versatility of the method in describing different symmetries and GB orientations. Moreover, we show how the periodicity of the defect structures is related to single Fourier modes and we illustrate how to exploit this connection to provide efficient simulations. The morphologies of the defect structures are found to correspond to the networks minimizing the GB energy as reported in the literature. The effect of different twist angles on the features of dislocation networks as well as on the GB energies are also discussed.

Afterwards, the closed dislocation networks forming spherical GBs due to rotated crystal inclusions are addressed. Their morphologies are discussed also pointing out the similarities with the defect networks of planar, twist GBs reported previously. The anisotropic shrinkage of rotated spherical grains and the connection with standard continuum theory are then discussed. Through the entire paper both fcc and bcc lattice symmetries are considered, proving the versatility of the method and the generality of the reported observations. It is worth mentioning that similar investigations adopting standard PFC were recently provided in Ref.[26] for bcc lattice symmetry only. This agreement further validates the coarse-grained approach considered here. Moreover, new results are shown for fcc symmetry and allow for the identification of general features occurring during the shrinkage of rotated grains.

The paper is organized as follows. In Sect. II the APFC approach is briefly illustrated, while the modeling and computational details developed for the investigations reported in the following sections are summarized in Sect. II A. Results concerning planar, twist GBs are reported in Sect. III. The morphologies and the shrinkage of spherical rotated crystals are shown and discussed in Sect. IV. Conclusion and remarks are summarized in Sect. V.

II. APFC MODEL

The standard PFC approach is based on the definition of a free energy, F_n, as function of the local atomic density, n[37]:

$$F_n = \int_\Omega \left[\frac{\Delta B_0}{2} n^2 + \frac{B_0^x}{2} n (1+\nabla^2)^2 n - \frac{t}{3} n^3 + \frac{v}{4} n^4 \right] d\mathbf{r}, \tag{1}$$

where ΔB_0, B_0^x, v and t are positive parameters controlling the properties of the system[37]. The coarse grained approach considered in this work consists in the so-called amplitude expansion[27–29] of the PFC model (APFC), where the atomic density is expressed as

$$n = n_0 + \sum_{j=1}^{N} \left[\eta_j(\mathbf{x},t) e^{i\mathbf{k}_j\cdot\mathbf{x}} + \eta_j^*(\mathbf{x},t) e^{-i\mathbf{k}_j\cdot\mathbf{x}} \right], \tag{2}$$

with $\mathbf{k}_j$ the N nonzero reciprocal-lattice vectors reproducing a specific lattice symmetry and n_0 the average density which can be set to zero without loss of generality[33]. For bcc lattice symmetry $N = 6$ and the $\mathbf{k}_j/k_0$ vectors read: $\mathbf{k}_1$=$(1,1,0)$, $\mathbf{k}_2$=$(1,0,1)$, $\mathbf{k}_3$=$(0,1,1)$, $\mathbf{k}_4$=$(0,1,\bar{1})$, $\mathbf{k}_5$=$(1,\bar{1},0)$, $\mathbf{k}_6$=$(\bar{1},0,1)$, with $k_0 = \sqrt{2}/2$. For fcc lattice symmetry $N = 7$ and the $\mathbf{k}_j/k_0$ vectors read: $\mathbf{k}_1$=$(\bar{1},1,1)$, $\mathbf{k}_2$=$(1,\bar{1},1)$, $\mathbf{k}_3$=$(1,1,\bar{1})$, $\mathbf{k}_4$=$(\bar{1},\bar{1},\bar{1})$, $\mathbf{k}_5$=$(2,0,0)$, $\mathbf{k}_6$=$(0,2,0)$, $\mathbf{k}_7$=$(0,0,2)$, with $k_0 = \sqrt{3}/3$. Further details can be found in Refs.[33,35].

In the APFC approach the state and the evolution of the system are described by the amplitude functions η_j, which are complex functions. The free energy functional of the APFC approach is then written in terms of η_j's.

Assuming that these functions vary on lengthscales much larger than the atomic spacing, the free energy reads

$$F = \int_\Omega \Big[\frac{\Delta B_0}{2} A^2 + \frac{3v}{4} A^4 + \sum_{j=1}^{N} \left(B_0^x |\mathcal{G}_j \eta_j|^2 - \frac{3v}{2} |\eta_j|^4 \right) + f^{\mathrm{s}}(\{\eta_j\}, \{\eta_j^*\}) \Big] d\mathbf{r}, \tag{3}$$

where $\mathcal{G}_j \equiv \nabla^2 + 2i\mathbf{k}_j \cdot \nabla$ and

$$A^2 \equiv 2 \sum_{j=1}^{N} |\eta_j|^2. \tag{4}$$

The parameters are set as follows: $B^x = 0.98$, $v = 1/3$, $t = 1/2$ and $\Delta B = 0.02$[33,35]. A^2 describes the phases of the system; it is constant for a bulk crystal, decreases at solid-liquid interfaces or at defects and vanishes in disordered or liquid phases. $f^{\mathrm{s}}(\{\eta_j\}, \{\eta_j^*\})$ are complex polynomials generated by the cubic and quartic terms in the free energy F_n, whose exact form depends on crystal symmetry as reported in Ref.[35]. The evolution laws for η_j's read

$$\frac{\partial \eta_j}{\partial t} = -|\mathbf{k}_j|^2 \frac{\delta F}{\delta \eta_j^*}, \tag{5}$$

with

$$\frac{\delta F}{\delta \eta_j^*} = \left[\Delta B_0 + B_0^x \mathcal{G}_j^2 + 3v \left(A^2 - |\eta_j|^2 \right) \right] \eta_j + \frac{\delta f^s(\{\eta_j\}, \{\eta_j^*\})}{\delta \eta_j^*}. \tag{6}$$

By means of η_j's, it is possible to account for distortion of the lattice. Indeed they can be generally written in the polar form as

$$\eta_j(\mathbf{r}) = \bar{\eta}_j e^{i\varphi_j(\mathbf{r}) \cdot \mathbf{r}}. \tag{7}$$

$\bar{\eta}_j$ can be determined by the minimization of the free energy functional assuming equal and constant amplitudes for each different $\mathbf{k}_j$ length, i.e. by considering a relaxed crystal[33,35]. The phase term $\varphi_j(\mathbf{r})$ can instead account for displacements of the lattice with respect to a reference state. In this work, we are interested in describing GBs between rotated, three-dimensional crystals. These systems can be described by setting a phase term that quantifies the difference between the reciprocal-lattice vectors in the rotated system, $\mathbf{k}_j^\theta$, and the original ones $\mathbf{k}_j$. This can be generally written as

$$\varphi_j(\mathbf{r}) = \delta \mathbf{k}_j(\theta) \Theta(d(\mathbf{r})), \tag{8}$$

with Θ the Heaviside function, $d(\mathbf{r})$ the signed distance from the interface between a rotated ($d(\mathbf{r}) > 0$) and an unrotated ($d(\mathbf{r}) < 0$) crystal, and $\delta \mathbf{k}_j(\theta) = \mathbf{k}_j^\theta - \mathbf{k}_j$. The latter, for a rotation of an angle θ around the $\hat{\mathbf{x}}$-axis, reads

$$\delta \mathbf{k}_j(\theta) = \left[k_j^y (\cos\theta - 1) - k_j^z \sin\theta \right] \hat{\mathbf{y}} + \left[k_j^y \sin\theta + k_j^z (\cos\theta - 1) \right] \hat{\mathbf{z}}. \tag{9}$$

Eqs. (7), (8) and (9) can then be used in order to specify specific rotations as function of coordinates. They will be adopted to set the initial condition for simulations. Notice that $\delta \mathbf{k}_j(\theta)$ directly defines the wavelength of the amplitude oscillations as $\lambda_i^j = 2\pi / [\delta \mathbf{k}_j(\theta)]_i$ with $i = x, y, z$.

A. Simulation and modeling details

The equations defined in (5) and (6) are solved by a Finite Element approach exploiting the toolbox AMDiS[38,39]. We used a semi-implicit time discretization scheme for each amplitude. The resulting N systems of second-order partial differential equations are then coupled by evaluating explicitly the terms originating from $f^{\mathrm{s}}(\{\eta_j\}, \{\eta_j^*\})$ which depend on more than one η_j. Mesh refinement and adaptivity are used in order to ensure the proper spatial discretization at defects. Conversely, a coarse mesh is sufficient to describe the long wavelength oscillations of amplitudes as well as constant values for unrotated crystals. The details of the numerical method, as well as the mesh-refinement criterion, are reported in Ref.[35].

The η_j's are initialized by Eqs. (7), (8) and (9), i.e. a rotation of crystals about the $\hat{\mathbf{x}}$-axis is set as illustrated in Fig. 1(a). Periodic Boundary Conditions (PBCs) are set for all the amplitudes. In order to simulate planar, twist GBs we set $d(\mathbf{r}) \equiv x$, having then a grain boundary with normal $\hat{\mathbf{x}}$ at $x = 0$. Due to PBCs a second GB is expected, that is shared between the periodic boundaries with normal along $\hat{\mathbf{x}}$. In the following only the GB at $x = 0$ will be shown.

We consider two orientations for the twist GBs. In particular, we consider rotations about [111] and [110] directions. For the former we set $\hat{\mathbf{x}}$ =[111], $\hat{\mathbf{y}}$ =[1$\bar{1}$0] and $\hat{\mathbf{z}}$ =[11$\bar{2}$]. For the latter we set $\hat{\mathbf{x}}$ =[110], $\hat{\mathbf{y}}$ =[$\bar{1}$10] and $\hat{\mathbf{z}}$ =[001]. Notice that some of the original $\mathbf{k}_j$ are aligned with the $\hat{\mathbf{y}}$ and $\hat{\mathbf{z}}$ axes, so that a small angle rotation would produce small components of $\delta \mathbf{k}_j(\theta)$ and, in turn, large wavelengths λ_i^j. In order to use PBCs, the size of the simulation domain along $\hat{\mathbf{y}}$ or $\hat{\mathbf{z}}$ should then be a multiple of all the λ_i^j with $i = y, z$ respectively and $j = 1, ..., N$. This would lead to very large computational domains and unfeasible simulations. To overcome this issue, a rotation of the simulation cell of an angle α, chosen in order to have the smallest of the $\delta \mathbf{k}_j(\theta)$ vector aligned with the boundaries, is then considered. This allows us to set the smallest sizes of the simulation domain, hereinafter referred to as S_i with $i = x, y, z$. In particular this holds true for domain sizes along the new $\hat{\mathbf{y}}$ and $\hat{\mathbf{z}}$ directions (now rotated by α), namely S_y and S_z. The

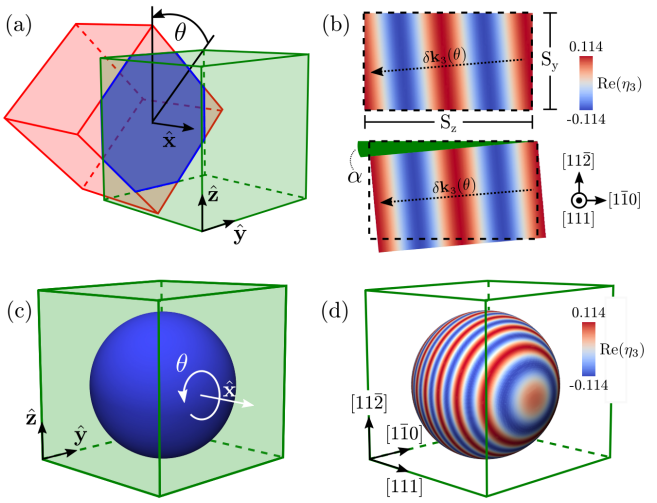

FIG. 1. Details about the simulation setup. (a) Schematics of a planar, twist GB. (b) yz cross-section for a crystal with fcc symmetry rotated about the [111] with $\theta = 10°$. The two panels show $\mathrm{Re}(\eta_3)$ with (below) and without (above) the rotation of the angle α, chosen to have $\delta\mathbf{k}_3(\theta)$ aligned to the boundaries. This allows for the smallest S_y and S_z to reproduce the dislocation network at the GB. (c) Schematics of a rotated, spherical crystal embedded in an unrotated crystal. (d) Illustration of the $\mathrm{Re}(\eta_3)$ for the initial condition leading to spherical GBs with $\theta = 10°$.

size S_x is arbitrary as it sets the distance between planar GBs. It is set to 50π. An example of this argument is shown in Fig. 1(b) for an fcc lattice. Two yz cross-sections of the simulation domain adopted to reproduce a (111) planar twist GB with $\theta = 10°$ are shown, with (below) and without (above) the rotation of the simulation domain of the angle α about the [111] direction. Notice that without such a rotation the values of $\mathrm{Re}(\eta_3)$ do not satisfy PBCs. To recover these conditions, a much larger simulation domain is required. Conversely, having $\delta\mathbf{k}_3$ parallel to the sides allows for using the domain with S_i as in Fig. 1(b) and PBCs. For the sake of simplicity, the dislocation networks will be shown upon a rotation of $-\alpha$ in order to have the boundaries aligned with the original frame of reference.

In order to simulate spherical, rotated crystal and, in turn, spherical GBs as shown in Fig. 1(c) we set $d(\mathbf{r}) \equiv R - |\mathbf{r}|$. It corresponds to a rotated crystal inclusion in an unrotated crystal. This allows us to set the domain size independently of the rotation of the crystals as η_j will not oscillate at the boundaries. In particular we set $R = 60\pi$ and $S_i = 140\pi$. The same orientations and frames of reference as for planar GBs are used. Fig. 1(d) shows $\mathrm{Re}(\eta_3)$ (as in Fig. 1(b)) for fcc lattice symmetry within the embedded crystal, rotated about the [111] direction.

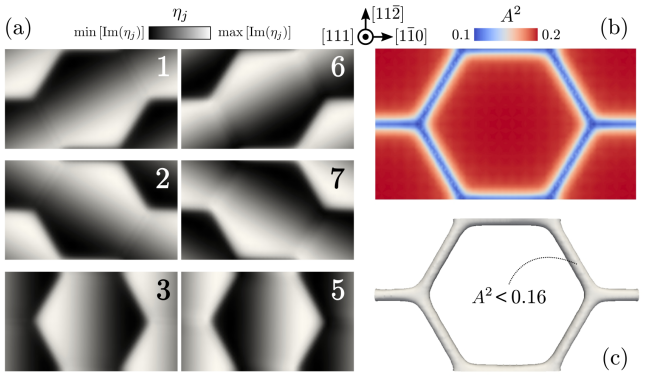

FIG. 2. Equilibrium condition for a (111) twist GB with fcc symmetry ($\theta = 10°$), reproduced by the APFC model. (a) $\mathrm{Im}(\eta_j)$ ($\mathrm{Im}(\eta_4) \sim 0$ not shown). Numbers correspond to the value of the index in $\mathbf{k}_j$. (b) A^2 from Eq. (4) computed from the amplitude functions illustrated in panel (a). (c) Dislocation network identified as region where $A^2 < 0.8\max(A^2)$.

Fig. 2 shows various aspects of the APFC simulations. The aforementioned procedure illustrated in Fig. 1(a) and Fig. 1(b) is used. Moreover, the relaxation of the initial condition is evaluated by integrating Eqs. (5) and (6) as in Ref.[35]. Fig. 2(a) illustrates the imaginary part of amplitudes η_j at the GB (i.e. the yz plane of the 3D domain at $x = 0$) with $\theta = 10°$ (after the $-\alpha$ rotation), with the corresponding value of the index j reported on each panel. Real parts (not shown) exhibit similar features. The solutions for η_j illustrated in Fig. 2(a) represent the amplitude of the Fourier modes to be used in Eq. (2) at the equilibrium. They directly reflect the features and symmetries of $\mathbf{k}_j$ vectors. Panels on the same row refer to η_j which have anti-parallel projections of $\mathbf{k}_j$ on the yz-plane. Indeed, the same features of the resulting fields are obtained with an opposite sign only. $\mathbf{k}_4$ is aligned to the rotation axis, so the components of $\delta\mathbf{k}_4$ are equal to zero, the initial condition for η_4 consists of a real function with $\eta_4 = \bar{\eta}_4$, and $\mathrm{Im}(\eta_4) \sim 0$, so that it is not shown in Fig. 2(a).

Fig. 2 also illustrates the steps adopted in order to recognize and show defects by means of solutions in terms of η_j fields. The order parameter A^2 is computed from the amplitudes by Eq. (4). As shown in Fig. 2(b), A^2 is constant except for localized regions. These regions correspond to defects of the crystal lattice[27–29] and in particular to the network of dislocations defining the GBs that will be discussed in the following. Therefore, a coarse-grained description is achieved, directly accounting for defects and thus describing the crystal lattice in an effective way. The results of simulations will be shown focusing on these dislocation networks, as illustrated in Fig. 2(c). In this figure, the three-dimensional region where $A^2 < 0.8\max(A^2)$ is reported. Notice that different features of the resulting dislocation network as in Fig. 2(c) are shared between some of the η_j's, revealing their contribution in determining the morphologies of GBs. Moreover, the system size (S_i) allows for sim-

ulating exactly one unit cell of the resulting dislocation network.

III. PLANAR GRAIN BOUNDARIES

In this section we show the results for dislocation networks at twist GBs simulated by APFC. The procedure described in Sect. II A is used to generate the initial configurations as shown in Fig. 2. Figs. 3 and 4 illustrate the results in terms of dislocation networks at GBs obtained for different orientations and lattice symmetries. Two twist angles θ, namely $\theta = 5°$ and $\theta = 10°$ are considered. Notice that angles can be chosen here in a continuous fashion as only long wavelength amplitudes have to be defined. The comparison between simulations with different θ shows that the dislocation networks at the GBs are preserved from a qualitative point of view, while the dislocation density increases when increasing the twist angle. Details concerning the dislocation network obtained for each specific symmetry and orientation will be discussed in the following. The size of the simulation cell in the plane perpendicular to the rotation axis is illustrated by a blue dotted line and a shaded area. Notice that the smaller the tilt the larger the simulation cell is, in agreement with the definition of λ_i^j. So that an intrinsic limit in simulation feasibility exists for very small angles. Solid thick lines illustrate the feature of the unit-cell for dislocation networks, which have a size corresponding to the simulation domain. The simulated networks are repeated 4 times (2×2) for $\theta = 5°$ and 16 times (4×4) for $\theta = 10°$ to illustrate the resulting dislocation pattern. As a check, the same dislocation networks have been obtained by simulating the entire domains reported in Fig. 3 and 4. Notice that a rotation of $-\alpha$ has been performed on the reported dislocation networks (see also Sect. II A).

Let us first focus on the twist GBs for the fcc symmetry. Fig 3(a) illustrates the dislocation network forming at the planar (111) boundary of two twisted fcc crystals. It consists of a hexagonal network formed by three sets of dislocation directions $\boldsymbol{\xi}_i$ (highlighted in Fig 3(a) by red dashed lines). When considering low angle twist boundaries, such a network made of dislocations with Burgers vectors $\mathbf{b} = a/2\langle 110\rangle$, with a the lattice spacing, is the most favorite according to energy minimization[40,41]. This corresponds, e.g., to what has been observed in twisted, Au (111) thin films[42]. For this system, it is known that a smaller number of dislocation sets with similar Burgers vectors would be enough to accommodate the misorientation but they would form four-fold dislocation junctions, instead of the three-fold junctions of Fig 3(a), and they do not correspond to the energy minimum (see the green solid line on the dislocation network obtained for $\theta = 10°$). Moreover, this holds true also for the dissociation of the junctions between dislocations forming additional triangular network[40]. Thus the method used here provides the minimum energy configurations.

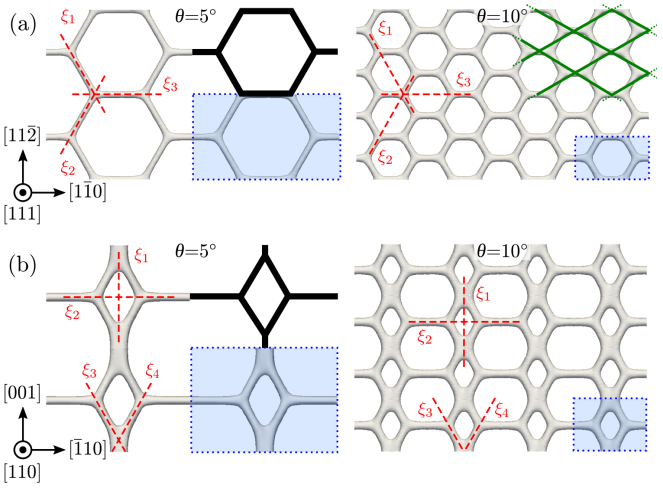

FIG. 3. Planar twist-GBs, fcc symmetry. Dislocation networks corresponding to $\theta = 5°$ (left) and $\theta = 10°$ (right) are reported. Blue dotted line and shaded areas illustrate the simulation domain for each case. Dislocation directions $\boldsymbol{\xi}_i$ are highlighted by red dashed lines. Solid black lines represent a schematics of the resulting dislocation networks. (a) (111) twist GB. Green solid lines in the $\theta = 10°$ panel illustrate the minimal set of dislocations accommodating the misorientation, still not minimizing the energy. (b) (110) twist GB.

Fig 3(b) illustrate the twist GB obtained at the planar (110) boundary between two fcc crystals. The resulting dislocation network is different than for the (111) twist GB. Here it is made by two sub-units, namely an irregular hexagon and a rhombus. As illustrated in the figure, four sets of dislocations (see $\boldsymbol{\xi}_i$) are present, still forming three-fold junctions as for the case reported in Fig 3(a). For (110) twist GBs many structures with almost equal energies are known[43,44]. However, in analogy with what discussed for the (111) twist GBs, the configuration in Fig. 3(b) can be considered as the most favorite one for small values of θ.

Fig. 4 shows the twist GBs for bcc symmetry. In particular, Fig. 4(a) shows the dislocation network forming at the planar (110) boundary between two twisted bcc crystals. An irregular hexagonal structure is obtained. Such a structure corresponds to what is observed, e.g., for Fe (110) crystals[45,46]. It consists of two dislocations with Burgers vector $\mathbf{b}_1 = a/2\langle 111\rangle$, along $\boldsymbol{\xi}_1$ and $\boldsymbol{\xi}_2$, which join forming a dislocation with Burgers vector $\mathbf{b}_2 = a\langle 100\rangle$ along $\boldsymbol{\xi}_3$. The angle between $\boldsymbol{\xi}_1$ and $\boldsymbol{\xi}_2$ is $\beta \gtrsim 90°$[46]. Similar to the case reported in Fig. 3, a possible configuration for (110) twist GBs for bcc lattice symmetry can consist in two sets of dislocations oriented along $\langle 112\rangle$ directions. This structure is reported by green solid lines in Fig. 4(a), superposed to the defects obtained with $\theta = 10°$. However, the result of APFC simulations corresponds to the expected configuration after forming a three-fold junction and represents the more stable configuration. As a further assessment of the re-

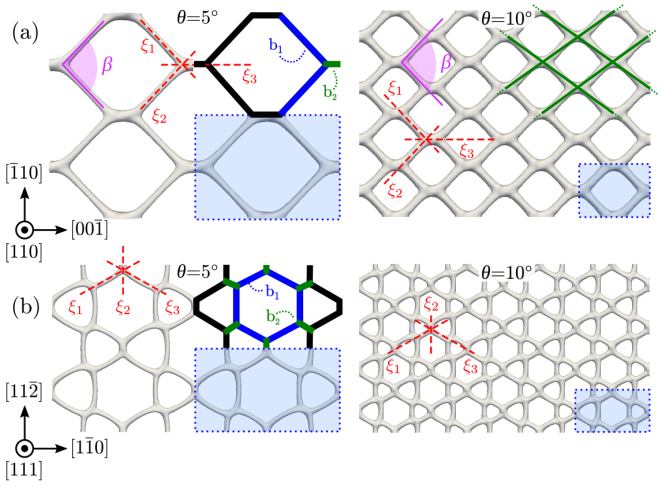

FIG. 4. Planar twist-GBs, bcc symmetry. Dislocation networks corresponding to $\theta = 5°$ (left) and $\theta = 10°$ (right) are shown. Blue dotted line and shaded areas illustrated the simulation domain for each case. Dislocation directions $\boldsymbol{\xi}_i$ are highlighted by red dashed lines. Solid lines represent the schematics of the resulting dislocation networks. They illustrate also the two different expected Burgers vectors: $\mathbf{b}_1 = a/2\langle 111\rangle$ (blue) and $\mathbf{b}_2 = a\langle 100\rangle$ (green). (a) (110) twist GB. The angle between $\boldsymbol{\xi}_1$ and $\boldsymbol{\xi}_2$, β, is also illustrate. Green solid lines in the $\theta = 10°$ panel illustrate the minimal set of dislocations accommodating the misorientation, still not minimizing the energy. (b) (111) twist GB.

ported results, similar structures have been obtained by MD[47] and recently by PFC simulations[26].

Fig 4(b) illustrates the dislocation network forming at the (111) planar interface between two twisted crystals. Another dislocation network is observed here with respect to the (110) twist GB. It is formed by two sets of hexagons and it is compatible with GBs having six dislocations with Burgers vector $\mathbf{b}_1$ for the hexagon at the center of the pattern, surrounded by other six hexagons formed by dislocations with Burgers vectors $\mathbf{b}_1$ and $\mathbf{b}_2$ as observed in Ref.[26] and illustrated in Fig 4(b).

The energies per unit area of the GB computed from Eq. 3, i.e. F/A with $A = 2S_yS_z$ (the factor 2 is included to account for the two GBs formed due to PBCs along the $\hat{\mathbf{x}}$ direction), as function of the tilt angle for the symmetries and the orientations of twist GBs considered so far, are shown in Fig. 5. A typical Read-Schockley behavior, namely corresponding to

$$E(\theta) = p\theta[q - \log(\theta)], \tag{10}$$

with $p, q > 0$, is observed[10]. The dashed lines in Fig. 5 are obtained by fitting the energy values by Eq. (10). Fcc GBs have higher energy per unit area than the bcc. Focusing on specific symmetries, we can also see that twist GBs with an orientation corresponding to the plane with higher packing fractions have lower energies. Indeed, $E^{\rm fcc}_{(111)} < E^{\rm fcc}_{(110)}$ and $E^{\rm bcc}_{(110)} < E^{\rm bcc}_{(111)}$. This is in agreement with what obtained with other methods as, e.g., in Refs.[48–50].

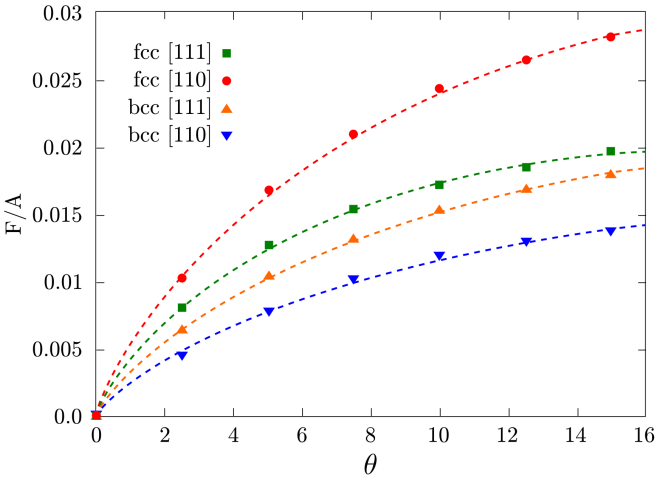

FIG. 5. Energy per unit area of the twist GBs as function of the twist angle. The symmetries and the GB orientations as considered in Fig. 3 and 4 are reported. Dashed lines are obtained as a fit of the simulation results by Eq. (10).

IV. SPHERICAL GRAIN-BOUNDARIES

In this section the APFC approach is exploited to describe the dislocation networks on spherical GBs, separating a rotated embedded crystal from an unrotated and relaxed lattice. Moreover, the shrinkage of the resulting GBs is discussed. The approach illustrated in Sect. II A by means of Figs. 1(c) and 1(d) is adopted.

The GB structure generated by a spherical, rotated inclusion in the crystal structure is expected to be similar to a twist GB in the region where the surface normal, $\hat{\mathbf{n}}$, of the rotated grain approaches the rotation axis. In directions perpendicular to $\hat{\mathbf{n}}$, pure tilt GBs are expected while mixed GBs are expected to form for orientations in between. The results of APFC simulations, after relaxing to a stationary shape for the defect network, are reported in Fig. 6. Fcc and bcc symmetries are considered. In analogy with the investigation illustrated in Sect. III, two different rotations about the [111] and [110] directions, both with $\theta = 5°$ and $\theta = 10°$, are considered. The unit-elements of the dislocation networks obtained for the corresponding planar, twist GBs are also illustrated by the gray insets with solid lines.

The results reported in Fig. 6 show that the GBs consist of closed dislocation networks. Two regions showing the peculiar networks corresponding to twist GBs are obtained for $\hat{\mathbf{n}}$ parallel and anti-parallel to the rotation axis. Such networks deform when moving away from such directions and they are made by elongated straight defects when approaching directions perpendicular to the rotation axes, typical of pure tilt GBs. The same qualitative dependence on the rotation angle illustrated previously for planar twist GBs is found. Notice that, although the

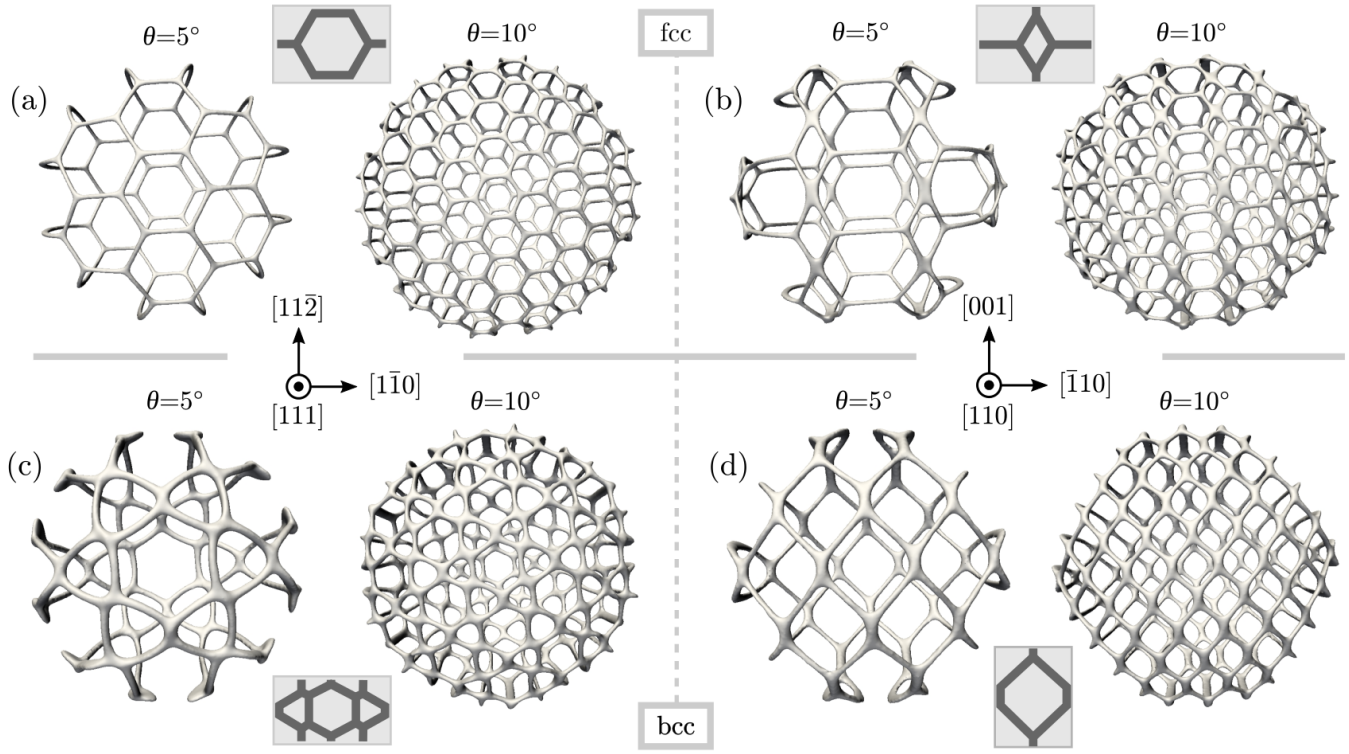

FIG. 6. Dislocation networks forming spherical GBs. A rotated inclusion, with radius of $\sim 60\pi$, is considered in each panel with a rotation of $\theta = 5°$ and $\theta = 10°$ about: (a) [111] direction for fcc symmetry, (b) [110] direction for fcc symmetry, (c) [111] direction for bcc symmetry, (d) [110] direction for bcc symmetry. The gray insets show the unit-cell of the dislocation networks found for planar twist GBs and closely resemble the structure of the spherical GBs where their normal approaches the rotation axis.

limiting case of twist/tilt GBs can be determined by energy and symmetry considerations and do not require, in principle, numerical simulations, the mixed GBs forming in between as well as the connecting dislocation networks are far from trivial and are obtained here by the same approach delivering planar GBs as in Sect. III. Moreover, no restrictions are present on the shape of the GBs, that can be selected arbitrarily.

The classical model for capillary-driven grain growth predicts a shrinkage of spherical GBs due to the curvature of the interface between rotated crystals[36]. If an isotropic surface energy is considered the shrinkage of a spherical grain can be fully described by the decrease of its radius, R, over time, t, such that $R^2 = R_{\text{ini}}^2 - \alpha t$, where R_{ini} is the initial radius and α is a constant. For real grains, the situation is much more complex, as the dislocation network shrinks as a function of time. Two dimensional MD and PFC simulations have shown for small-angle misorientations that this leads to an increase of the interface energy and a rotation of the grain that increases the mismatch orientation[51–54]. This increase in mismatch orientation occurs as the dislocations forming the GB come closer together. Despite these differences the dynamics of the radius (or area) has been shown to obey the relationship described above.

The situation is more interesting in three dimensional systems as the anisotropic nature of interface energy and mobility must be taken into account. This implies that the shrinkage of the grain is more complex as the velocity of the shrinkage depends on the local orientation of the GB. This leads to the presence of preferential orientation for GBs. An accurate continuum description of shapes originating from anisotropic interface energies and their evolution generally requires advanced methods[55] as well as the proper mapping of GB energies[14]. The APFC approach adopted here contains inherently such information such as anisotropic interface energy at GBs (see Fig. 5) and specific dislocation structures as discussed in Sect. III, although it does not explicitly account for atoms in the crystal lattice.

Long-timescale numerical simulations using the APFC model allow for the investigation of the shrinkage of the dislocation networks formed at an initially spherical grain. Fig. 7 illustrates the GB shrinkage achieved for the cases reported in Fig. 6 with $\theta = 5°$. For each case, two views are shown, illustrating the shrinkage of the grains parallel and perpendicular to the rotation axis. A common trend independent of the crystal symmetry and orientation appears: the shrinkage in the direction of the rotation axis is faster than in the other directions. Moreover, some small rotations of the grains occur during their shrinkage. In Ref.[26] this behavior was obtained (from

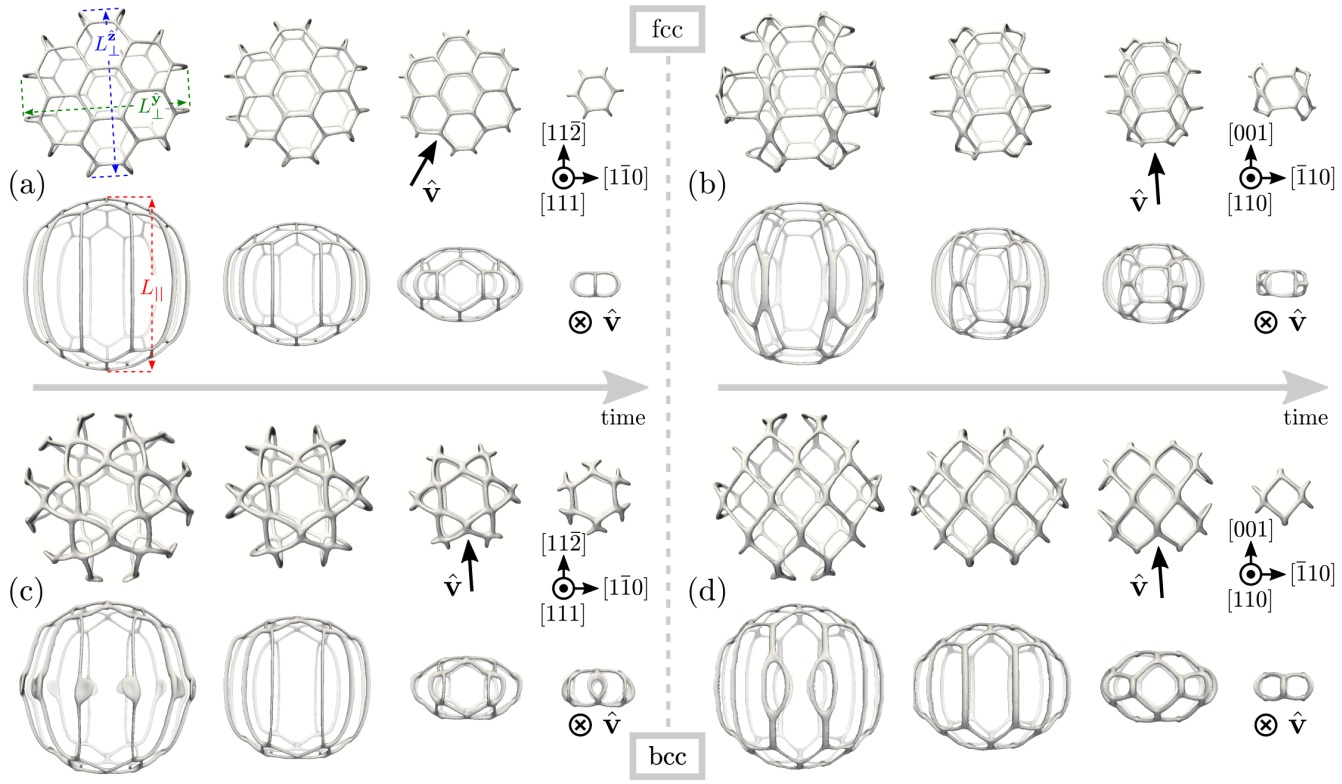

FIG. 7. Shrinkage of spherical GBs for different symmetries with $\theta = 5°$. The views aligned (top) and perpendicular (bottom) to the rotation axis are shown (as also illustrated by $\hat{\mathbf{v}}$). (a) fcc symmetry, rotation about the [111] direction. (b) fcc symmetry, rotation about the [110] direction. (c) bcc symmetry, rotation about the [111] direction. (d) bcc symmetry, rotation about the [110] direction. Panel (a) illustrates also the width of the embedded crystal along different directions, namely $L_{||}$, $L_{\perp}^{\hat{\mathbf{y}}}$ and $L_{\perp}^{\hat{\mathbf{z}}}$.

atomistic calculations with the PFC model) for the bcc lattice symmetry and attributed to the anisotropic distribution of dislocations at the GBs. Similar to that work, we also observe the same results for the dynamics of the dislocation networks in terms of dislocation type and disappearance. This comparison further validates the theoretical and computational approach adopted here. Moreover, we also observe this qualitative behavior for the fcc case.

Deeper insights on the anisotropic shrinkage can be found in Fig. 8. Here, the widths, L, of the shrinking GBs are extracted along the rotation axis, $L_{||}$, and along two directions in the plane perpendicular to the rotation axis, $L_{\perp}^{\hat{\mathbf{y}}}$ and $L_{\perp}^{\hat{\mathbf{z}}}$ namely evaluated along the $\hat{\mathbf{y}}$ and $\hat{\mathbf{z}}$ directions of different frames of reference as specified in Sect. II A (see also Fig. 7). As seen in Fig. 8 an initial transient phase can be observed corresponding to the relaxation of the initial condition and the formation of defect networks. Afterwards, a smaller width along the rotation axis ($L_{||}$) is observed for all the cases. At the end of the process when all the widths approach zero, a slightly faster evolution is observed. This corresponds to the final annihilation of the dislocations and the disappearance of the grains. $L_{||}$ is found to decrease linearly with nearly the same velocity during the entire process. Conversely, after the formation of the dislocation networks, both $L_{\perp}^{\hat{\mathbf{y}}}$ and $L_{\perp}^{\hat{\mathbf{z}}}$ show an almost linear behavior as well but with a velocity significantly slower than $L_{||}$. This stage can be ascribed to a stronger tendency to shrink the two-dimensional dislocation networks having a normal perpendicular to the rotational axis rather than the dislocation network corresponding to twist GBs. When approaching the final disappearance of the grain, a sudden increase of the velocity along $\hat{\mathbf{y}}$ and $\hat{\mathbf{z}}$ directions is observed. This change in the shrinking rate, in the presence of an almost constant decrease of $L_{||}$, allows for having a closed dislocation network preventing the formation of a high energy configuration such as a plate-like (2D) embedded crystal. Indeed, this would exhibit too large curvatures of the GB, that would correspond to a too high interfacial energy between the rotated inclusion and the unrotated crystal. Notice that, although a good description of the defects is achieved, the position of atoms during the annihilation of defects are not expected to be carefully described by the APFC approach.

In Ref.[26] a linear scaling of the GBs area during the evolution has been also found recovering the prediction of the classical theory[36]. From the data in Fig. 8, the surface area of the grains can be computed by assuming an ellipsoidal shape where the width of the grains is rep-

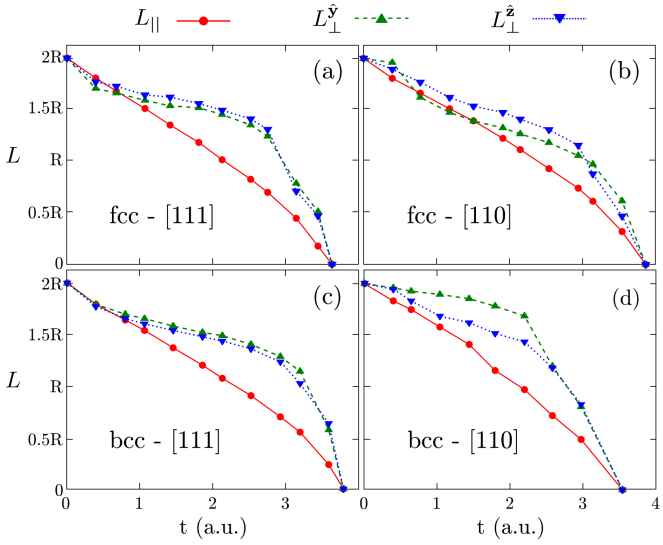

FIG. 8. Widths of the embedded rotated crystal over time, evaluated along the rotation axis, $L_{||}$, as well as along $\hat{\mathbf{y}}$ and $\hat{\mathbf{z}}$ of the specific frame of reference, namely $L_\perp^{\hat{\mathbf{y}}}$ and $L_\perp^{\hat{\mathbf{z}}}$. The four panels corresponds to the cases illustrated in Fig. 7.

resented by its axes. In particular, the surface area can be approximated by the Knud-Thomsen formula,

$$A = \frac{\pi}{3^{1/p}} \left[\left(L_{||} L_\perp^{\hat{\mathbf{y}}} \right)^p + \left(L_{||} L_\perp^{\hat{\mathbf{z}}} \right)^p + \left(L_\perp^{\hat{\mathbf{y}}} L_\perp^{\hat{\mathbf{z}}} \right)^p \right]^{1/p}, \tag{11}$$

with $p = 1.6075$. The corresponding areas normalized by the initial surface of the embedded spherical grain $A_{\text{ini}} = 4\pi R^2$ with $R = 60\pi$ are reported in Fig. 9.

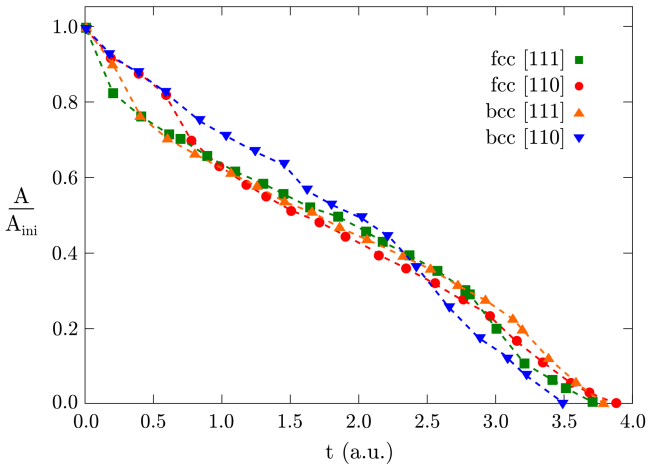

FIG. 9. Surface area of the shrinking crystals of Fig. 7 approximated as an ellipse having $L_{||}$, $L_\perp^{\hat{\mathbf{y}}}$ and $L_\perp^{\hat{\mathbf{z}}}$ as axes.

The decrease of the surface area of the grains over time is nearly linear for all the considered cases. Small deviations are observed only in the first and last stages corresponding to the defect formation and to the final disappearance of the grain. Moreover, from both Figs. 8 and 9 one can notice that the duration of the entire shrinkage process is similar even considering different symmetries and orientation of the GB. This evidence is in agreement with the results reported by PFC simulations in Ref.[26] concerning bcc lattice with different rotation axes. The dynamics of fcc rotated grains are then found to follow a very similar kinetic pathway, characterized by an anisotropic shrinkage with smaller $L_{||}$ and a similar timescale towards the disappearance of the rotated inclusion.

It is worth mentioning that the considered APFC approach does not include the effects of the dynamics mediated by phonons. Such a contribution may play a role when accounting for fast coarsening dynamics, providing correction to the shrinking rate which may be dependent on the lattice symmetry[56]. However, we expect the main qualitative observations to remain unaltered also in this regime, while conclusion reached by this study still hold true quantitatively for relatively slow processes.

V. CONCLUSIONS

In this work, we illustrated how the APFC approach can be adopted to provide a detailed coarse-grained, three-dimensional description of dislocation networks at GBs. Their morphology and evolution have been simulated by means of the evaluation of fields (namely, the complex amplitudes η_j) varying on larger lengthscales than the lattice spacing. Thus, a spatial resolution typically larger than the one used in atomistic approaches can be used to provide information about GBs on large systems and long timescales. Moreover, the extended defects forming at GBs can be directly identified by a scalar order parameter, A^2, which can be also exploited to modify and control defect properties[35]. The method has been shown to tackle fcc and bcc lattice symmetries without major changes. Different rotations and GBs orientations can be also considered without any restriction as shown by the reported simulations.

The results on planar, twist GBs provided an assessment of the validity of the approach used in this work for obtaining GB morphologies. In particular, the fine structures made of dislocations were shown to be directly accessible and consistent with well-known results obtained by symmetry considerations, energy minimization and other simulation methods. Notice that the relevant case of pure-twist GBs has been addressed but no restrictions are present for the simulation of planar, pure-tilt or mixed GBs. The dislocation networks obtained in the case of spherical GBs show the possibility to account for arbitrary GBs geometries, without loss of descriptive capability and accuracy.

The dynamics of dislocation networks at GBs during the shrinkage of embedded rotated crystals was also addressed. The importance of this investigation is two-fold. First, the dynamics of defects achieved by APFC simulation is found to reproduce recent results obtained by

PFC simulations accounting for bcc lattice symmetries[26], thus further validating the general APFC approach as a coarse-grained description of the PFC model. In particular, the peculiar anisotropic shrinkage of spherical rotated grains is reproduced with a linear decrease of the interface between rotated and unrotated crystal. Second, the approach allows for simulating and analyzing grain shrinkage for fcc symmetries. The dynamics of spherical GBs in fcc crystals is found to occur with very similar features with respect to bcc crystals. Specifically, the feature of anisotropic shrinkage observed for bcc both here and in Ref.[26] are then found to be general and independent of the lattice symmetry as well as of the rotation axis, even accounting for the different dislocation networks forming in each case. This unveils the generality of the observed behaviors and deepens the knowledge about GBs dynamics.

This work paves further the way to detailed investigations of 3D systems by APFC including also other physical contributions already shown to be correctly modeled by this approach in 2D such as binary systems[33,34] or the presence of both GBs and compositional domains[30,31]. Further work will be devoted to the optimization of the numerical approach in order to provide even more efficient calculations to enable simulations of grain growth in polycrystalline materials, similar to[57] in 2D.

ACKNOWLEDGEMENTS

M.S. acknowledges the support of the Postdoctoral Research Fellowship awarded by the Alexander von Humboldt Foundation. R.B. and A.V. acknowledge the financial support from the German Research Foundation (DFG) under grant SPP 1959. K.R.E. acknowledges financial support from the National Science Foundation under grant No. DMR1506634. The computational resources were provided by ZIH at TU Dresden and by the Jülich Supercomputing Center within the Project No. HDR06.

* marco.salvalaglio@tu-dresden.de

[1] A. P. Sutton and W. Baluffi, eds., *Interfaces in Crystalline Materials* (Oxford University Press, New York,, 1995).
[2] M. C. Demirel, A. P. Kuprat, D. C. George, and A. D. Rollett, Phys. Rev. Lett. **90**, 016106 (2003).
[3] V. Randle, Acta Mater. **52**, 4067 (2004).
[4] A. Rollett, G. Rohrer, and R. Suter, MRS Bulletin **40**, 951 (2015).
[5] J. P. Hirth and J. Lothe, *Theory of Dislocations*, 2nd ed. (John Wiley & Sons, New York, 1982).
[6] K. Merkle and D. Wolf, MRS Bulletin **15**, 42 (1990).
[7] C. R. M. Grovenor, J. Phys. C: Solid State Phys. **18**, 4079 (1985).
[8] D. M. Duffy, J. Phys. C: Solid State Phys. **19**, 4393 (1986).
[9] M. Haruta and H. Kurata, Sci. Rep. **2**, 252 (2012).
[10] W. T. Read and W. Shockley, Phys. Rev. **78**, 275 (1950).
[11] R. Kobayashi, J. a. Warren, and W. Craig Carter, Physica D **140**, 141 (2000).
[12] I. Steinbach and F. Pezzolla, Physica D **134**, 385 (1999).
[13] S. G. Kim, D. I. Kim, W. T. Kim, and Y. B. Park, Phys. Rev. E **74**, 061605 (2006).
[14] H.-K. Kim, S. G. Kim, W. Dong, I. Steinbach, and B.-J. Lee, Model. Simul. Mater. Sci. Eng. **22**, 034004 (2014).
[15] J. Jung, J. I. Yoon, J. G. Kim, M. I. Latypov, J. Y. Kim, and H. S. Kim, npj Computational Materials **3**, 21 (2017).
[16] D. Farkas, J. Phys. Condens. Matter **12**, R497 (2000).
[17] Y. Mishin, M. Asta, and J. Li, Acta Mater. **58**, 1117 (2010).
[18] M. I. Mendelev, C. Deng, C. A. Schuh, and D. J. Srolovitz, Model. Simul. Mater. Sci. Eng. **21**, 045017 (2013).
[19] M. P. Anderson, G. S. Grest, and D. J. Srolovitz, Philos. Mag. B **59**, 293 (1989).
[20] Q. Yu and S. K. Esche, Materials Letters **57**, 4622 (2003).
[21] K. R. Elder, M. Katakowski, M. Haataja, and M. Grant, Phys. Rev. Lett. **88**, 245701 (2002).
[22] K. R. Elder and M. Grant, Phys. Rev. E **70**, 051605 (2004).
[23] H. Emmerich, H. Löwen, R. Wittkowski, T. Gruhn, G. I. Tóth, G. Tegze, and L. Gránásy, Adv. Phys. **61**, 665 (2012).
[24] A. Adland, A. Karma, R. Spatschek, D. Buta, and M. Asta, Phys. Rev. B **87**, 024110 (2013).
[25] J. Berry, N. Provatas, J. Rottler, and C. W. Sinclair, Phys. Rev. B **89**, 214117 (2014).
[26] A. Yamanaka, K. McReynolds, and P. W. Voorhees, Acta Mater. **133**, 160 (2017).
[27] N. Goldenfeld, B. P. Athreya, and J. A. Dantzig, Phys. Rev. E **72**, 020601 (2005).
[28] B. P. Athreya, N. Goldenfeld, and J. A. Dantzig, Phys. Rev. E **74**, 011601 (2006).
[29] N. Goldenfeld, B. P. Athreya, and J. A. Dantzig, J. Stat. Phys. **125**, 1015 (2006).
[30] P.-A. Geslin, Y.C. Xu, and A. Karma, Phys. Rev. Lett. **114**, 105501 (2015).
[31] Y.C. Xu, P.-A. Geslin, and A. Karma, Phys. Rev. B **94**, 144106 (2016).
[32] C. Hüter, J. Neugebauer, G. Boussinot, B. Svendsen, U. Prahl, and R. Spatschek, Continuum Mech. Thermodyn. **29**, 895 (2017).
[33] K. R. Elder, Z.-F. Huang, and N. Provatas, Phys. Rev. E **81**, 011602 (2010).
[34] K. R. Elder and Z.-F. Huang, J. Phys. Condens. Matter **22**, 364103 (2010).
[35] M. Salvalaglio, R. Backofen, A. Voigt, and K. R. Elder, Phys. Rev. E **96**, 023301 (2017).
[36] R. Doherty, D. Hughes, F. Humphreys, J. Jonas, D. Jensen, M. Kassner, W. King, T. McNelley, H. McQueen, and A. Rollett, Mater. Sci. Eng. A **238**, 219 (1997).
[37] K. R. Elder, N. Provatas, J. Berry, P. Stefanovic, and M. Grant, Phys. Rev. B **75**, 064107 (2007).
[38] S. Vey and A. Voigt, Comput. Visual. Sci. **10**, 57 (2007).
[39] T. Witkowski, S. Ling, S. Praetorius, and A. Voigt, Adv. Comput. Math. **41**, 1145 (2015).

[40] R. F. Scott and P. J. Goodhew, Philos. Mag. A **44**, 373 (1981).
[41] J. T. M. De Hosson and V. Vitek, Philos. Mag. A **61**, 305 (1990).
[42] T. Schober and R. W. Balluffi, Philos. Mag. **20**, 511 (1969).
[43] K. W. Ingle and A. G. Crocker, Philos. Mag. A **41**, 713 (1980).
[44] J.D. Rittner and D.N. Seidman, Phys. Rev. B **54**, 6999 (1996).
[45] S. M. Ohr and D. N. Beshers, Philos. Mag. **8**, 1343 (1963).
[46] Y. Chou, Mater. Sci. Eng. **10**, 81 (1972).
[47] J. Yang, Y. Nagai, M. Hasegawa, and Y. Osetsky, Philos. Mag. **90**, 991 (2010).
[48] D. Udler and D. N. Seidman, Phys. Rev. B **54**, 11133 (1996).
[49] B. Runnels, I. J. Beyerlein, S. Conti, and M. Ortiz, J. Mech. Phys. Solids **89**, 174 (2016).
[50] B. Runnels, I. J. Beyerlein, S. Conti, and M. Ortiz, J. Mech. Phys. Solids **94**, 388 (2016).
[51] V. Heinonen, C. V. Achim, K. R. Elder, S. Buyukdagli, and T. Ala-Nissila, Phys. Rev. E **89**, 032411 (2014).
[52] K.-A. Wu and P. W. Voorhees, Acta Mater. **60**, 407 (2012).
[53] J. W. Cahn and J. E. Taylor, Acta Mater. **52**, 4887 (2004).
[54] J. W. Cahn, Y. Mishin, and A. Suzuki, Philos. Mag. **86**, 3965 (2006).
[55] M. Salvalaglio, R. Backofen, R. Bergamaschini, F. Montalenti, and A. Voigt, Cryst. Growth Des. **15**, 2787 (2015).
[56] V. Heinonen, C. V. Achim, J. M. Kosterlitz, S.-C. Ying, J. Lowengrub, and T. Ala-Nissila, Phys. Rev. Lett. **116**, 024303 (2016).
[57] R. Backofen, K. Barmak, K. Elder, and A. Voigt, Acta Mater. **64**, 72 (2014).